

Machine learning assisted identification of homobilayer sliding ferroelectrics with large out-of-plane polarization and low sliding energy barriers

Xian Wang,^{1,*} Yifan Li,^{2,*} Ying Zhang^{1,3,4}, Peng Wang^{1,5}, Yi-Ming Zhao^{1,2}, Jun Zhou^{1,6}, Jie Yang,⁷ Xuesen Wang¹, and Lei Shen^{1,2,4,†}

¹*Department of Physics, National University of Singapore, Singapore 117551, Singapore*

²*Department of Mechanical Engineering, National University of Singapore, Singapore 117575, Singapore*

³*Department of Electrical and Computer Engineering, National University of Singapore, Singapore 117576, Singapore*

⁴*National University of Singapore (Chongqing) Research Institute, Chongqing 401123 China*

⁵*College of Electronic and Information Engineering, Shandong University of Science and Technology, Qingdao 266590, China*

⁶*Institute of Materials Research and Engineering (IMRE), Agency for Science,*

*Technology and Research (A*STAR6), Singapore 138634, Singapore*

⁷*Key Laboratory of Material Physics, Ministry of Education, School of Physics, Zhengzhou University, Zhengzhou 450001, China*



(Received 23 October 2024; revised 9 February 2025; accepted 21 February 2025; published 10 March 2025)

Two-dimensional (2D) ferroelectric materials hold great promise for ultrahigh-density data storage and ultrafast memory applications in flexible or wearable electronic devices. Because of depolarizing field effects and high-energy barriers for switching, only a handful of 2D ferroelectrics have been reported experimentally, such as In_2Se_3 and CuInP_2S_6 . Through high-throughput calculations we identified a catalog of 25 synthesizable sliding ferroelectrics with large out-of-plane polarization and low sliding energy barriers. The high-throughput process started with 6351 monolayer materials in 2DMATPEDIA, narrowed down to 79 monolayer semiconductors with honeycomb structures, leading to the construction of 474 homobilayers sliding ferroelectrics, and ultimately identifying 25 high-performance 2D sliding ferroelectrics. Using big-data analysis and machine learning, we also revealed strong correlations between polarization and key physical properties, especially a hidden factor of *effective* van der Waals radius, which has been overlooked in previous fewer-sample studies. Based on these mechanistic insights, we proposed machine learning descriptors for predicting sliding ferroelectric properties.

DOI: [10.1103/PhysRevB.111.094106](https://doi.org/10.1103/PhysRevB.111.094106)

I. INTRODUCTION

The widespread use of silicon-based random-access memories (RAMs) faces significant challenges as integrated circuit sizes downscale to the nanoscale [1,2]. There is an urgent need for semiconductor materials with suitable band gaps, low-power dissipation, remarkable logic switching, and distinguished electronic performance across RAMs and photoelectric applications [3–6]. Ferroelectric RAMs offer promising solutions by providing nonvolatile memory with distinct “0” and “1” states. However, traditional nonlayered ferroelectrics (FE) are typically insufficient for high-density data storage (HDDS), while their vertical FE vanishes below a critical film thickness due to the depolarizing field [7,8]. In contrast, vertical FE has the capability to achieve HDDS with minimal quantum tunneling and power dissipation [9,10].

In recent years, two-dimensional (2D) ferroelectric materials have attracted remarkable attention for their various potential applications in ultrafast and high-density information storage, triboelectric nanogenerators, field-effect transistors, and electromechanical devices [11–14]. These applications benefit from reversible spontaneous electric polarization,

especially in materials exhibiting out-of-plane polarization (OOP), which aligns well with the requirements of technologies relying on ferroelectric polarizability perpendicular to the plane [15–17]. Nevertheless, achieving this excellent property in conventional FE remains challenging due to surface-depolarizing fields and high activation barriers for switching [8,18]. Over the past decade, most subnanometer ferroelectric materials in the 2D realm have been achieved through the physical exfoliation of layered materials into monolayer or few-layer forms [19,20]. However, experimental confirmation of OOP has been limited, with successful demonstrations achieved in CuInP_2S_6 [21], $\alpha\text{-In}_2\text{Se}_3$ [22], and $1T\text{-MoTe}_2$ [23]. Theoretically, a high-throughput computational search of 252 ferroelectric 2D materials identified only 8 materials with OOP [24], indicating that materials with intrinsic OOP are rare in 2D materials.

Beyond these naturally occurring ferroelectric 2D materials, Wu *et al.* [25] introduced a new type of 2D ferroelectrics driven by interlayer sliding, offering a promising avenue for inducing out-of-plane ferroelectricity in 2D materials derived from centrosymmetric nonpolar counterparts. This unique phenomenon involves reversible translational sliding of one monolayer relative to the other, distinguishing it from traditional ferroelectrics as it offers a novel means of switching ferroelectric polarization [3,26,27]. Additionally, sliding ferroelectrics often exhibit temperature-independent

*These authors contributed equally to this work.

†Contact author: shenlei@nus.edu.sg

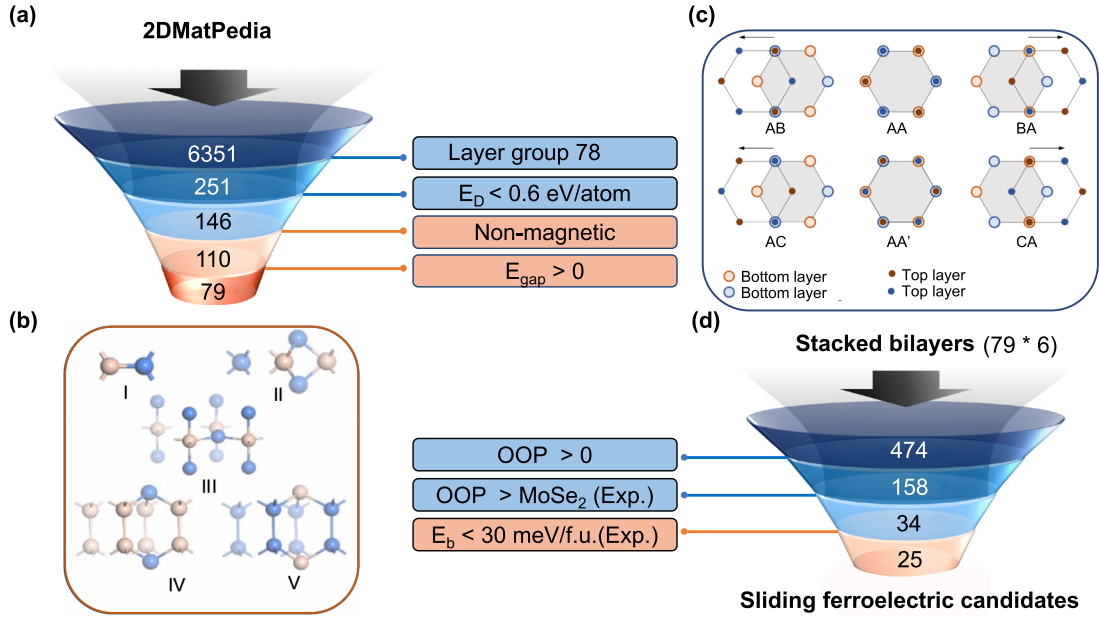


FIG. 1. Overall screening workflow for identifying sliding ferroelectric candidates with large out-of-plane ferroelectric polarization (OOP) and small sliding energy barriers (E_b). (a) The prescreening process from 2DMATPEDIA. Seventy-nine 2D materials are screened, 22 of which have been experimentally synthesized. (b) The 79 monolayer materials are grouped into five categories based on their geometric structures. (c) Six stacking patterns of a bilayer structure with layer group 78. (d) The screening process from the 79×6 bilayer structures to the 25 sliding ferroelectric candidates with large OOP and small E_b .

characteristics, including polarization stability across a broad temperature range, extending to room temperature [28]. The search for realistic 2D materials with strong sliding FE will help drive the practical applications of these materials. Sliding FE has been explored through first-principles calculations in various binary materials, including BY ($Y = \text{P, As, Sb}$), XN ($X = \text{Al, Ga, In}$), and ZC ($Z = \text{Si, Ge, Sn}$) [25,29], MoS_2 [30], WTe_2 [31], VS_2 [32], ZrI_2 [33], etc. Since 2017, many experimental studies have demonstrated sliding FE in a range of 2D materials, including XY_2 ($X = \text{Mo, W}$ and $Y = \text{S, Se}$) [34–36], WTe_2 [37,38], and MoTe_2 [39], $h\text{-BN}$ [40,41], ReS_2 [42], β - and γ - InSe [43–46], γ - GaSe [47]. However, experimentally realized sliding ferroelectric materials remain scarce. Thus, further theoretical explorations of materials with strong sliding FE and suitable switching energy barriers are needed to provide deeper insights for experimental research [48,49].

Pakdel *et al.* [50] utilized the Computational 2D Materials Database (C2DB) to perform high-throughput computations on the change in out-of-plane polarization potential ($\Delta\Phi_P$) in nonmagnetic bilayers, predicting their potential for slidetrionics applications. In this work, we combine the 2DMATPEDIA database [51] and experimental data of monolayer 2D materials, particularly XY_2 ($X = \text{Mo, W, Hf, Ti, Cr, Zr}$ and $Y = \text{S, Se, Te}$) [52], $h\text{-BN}$ [53], InSe [43,45,54,55], GaSe [47,56], and GaTe [57], to perform high-throughput density-functional theory (DFT) calculations to predict the OOP. These calculations systematically screen promising honeycomb homobilayers candidates that exhibit strong sliding FE and low sliding energy barriers. Meanwhile, by integrating machine learning (ML) with DFT results, we identify the key features that influence ferroelectric polarization and energy barriers. This combined approach provides a robust framework for ana-

lyzing and optimizing sliding FE materials, deepening our understanding of fundamental FE mechanisms, accelerating the discovery of sliding FE materials and advancing their practical applications.

II. METHODS

A. Materials prescreening in 2DMATPEDIA

We first conducted a comprehensive screening of semiconductor materials sourced from our 2DMATPEDIA database, which contains over 6000 2D materials [51]. Our selection criteria targeted nonmagnetic semiconducting materials by layer group 78 with honeycomb structures [58], and decomposition energies below 0.6 eV per atom as reported in other studies [25,29]. This screening process results in 79 2D materials, as illustrated in Fig. 1. More than 20 experimentally synthesized monolayer materials are included. According to their structural characteristics, five distinct types are classified with 12, 32, 13, 15, and 7 materials in types I to V, respectively (Fig. 1). Type I (XY) has the $h\text{-BN}$ -like structure [40] with a honeycomb lattice comprising alternating X and Y atoms. Type II (XY_2), analogous to $2H\text{-MoS}_2$ [34], represents materials where each X atom layer is sandwiched between two Y atomic layers, with each X atom surrounded by six Y atoms, forming a hexagonal ring with alternating X and Y atoms (when projected in the plane). In type III (XY_3), the crystal structure features X atoms covalently bonded to three Y atoms, forming tetrahedral structures that share edges to create hexagonal ring structures, such as AsI_3 [59]. Type IV, as exemplified by $\beta\text{-InSe}$ [45,55] and $\gamma\text{-InSe}$ [43,44], represents materials with a crystal structure where X atoms form covalent bonds with three Y atoms, arranged in trigonal coordination geometry. Within each layer, X atoms form hexagonal rings

with alternating Y atoms buckled out of the plane, and these layers stack with X - X bonding. Type V (XY) has the same chemical formula as type IV but with the positions of X and Y atoms exchanged, so that the layers stack with Y - Y bonding.

For constructing homobilayers on the basis of the 79 materials, six different stacking patterns are considered as shown in Fig. 1. The AA stacking configuration is the simplest bilayer stacking arrangement, where each atom in the top layer is directly above the corresponding atom in the bottom layer. AA' stacking refers to a configuration where the Y/X atom of the top layer is aligned directly above the Y/X atom of the bottom layer. AC/CA stacking describes a configuration where the Y/X atom of the top layer is positioned directly above the Y/X atom of the bottom layer, while the X/Y atom of the top layer is located directly over the center of a hexagon in the bottom layer. Finally, the AB/BA arrangement refers to a configuration in which the Y/X atom of the top layer is aligned directly above the center of a hexagon in the bottom layer, while the X/Y atom of the top layer is positioned directly over the Y/X atom of the bottom layer.

B. High-throughput calculations

All the first-principles calculations were conducted using the Vienna *Ab initio* Simulation Package (VASP) [60,61] within DFT framework, employing the projector augmented-wave method [62]. The Perdew-Burke-Ernzerhof (PBE) parametrization of the generalized gradient approximation was utilized to handle the exchange and correlation functional [63]. A plane-wave basis energy cutoff was employed to be 600 eV. Electronic minimization was performed with a tight convergence criterion of 10^{-6} eV, while ionic relaxation utilized a force tolerance of 0.005 eV/Å for each ion. A minimum vacuum region of 20 Å was applied to separate the periodically repeated bilayers. Brillouin-zone sampling employed a Γ -centered $15 \times 15 \times 1$ Monkhorst-Pack k -point mesh [64] to ensure convergence across all materials. Energy barriers for various kinetic processes were determined by employing the climbing image nudged elastic band (CI-NEB) method [65]. Additionally, van der Waals (vdW) corrections were included, parametrized within the DFT-D3 Grimme method [66]. Ferroelectric polarizations, with consideration of dipole correction, was evaluated using the Berry-phase method [67]. We validated our PBE-D3 method on previously reported sliding ferroelectrics, including h -BN, SiC, InSe, ZnO, and MoS₂ [17,25,29,34]. Figure S1 in Supplemental Material [68] shows that the method without dipole correction usually overestimates the polarization. Hence, the PBE-D3 method was adopted with dipole correction for computing OOP in this work.

C. Machine learning techniques

On the basis of DFT calculation results, we employed ML techniques to identify crucial features, influencing ferroelectric polarizations and energy barriers. The dataset includes several DFT-calculated properties, such as interlayer charge transfer, electron localization functions, relative electronegativity, interlayer distances, covalent bond lengths, vdW radii, and lattice parameters. These properties were used as input

features for the ML model. We then constructed a multilayer perceptron (MLP) predictive model to learn and predict these features [69]. The MLP architecture consisted of an input layer corresponding to the number of input features, followed by three hidden layers with 128, 64, and 32 neurons, respectively, each using rectified linear unit activation functions. Dropout regularization (20%) was applied after each hidden layer to prevent overfitting. The output layer used a linear activation function to predict the target values. The model was trained using the ADAM optimizer with a learning rate of 0.001 and a mean-squared error loss function. Training was conducted using 60% of the data, with 40% reserved for validation, and the model was trained for 100 epochs with a batch size of 32. Early reserve for validation was applied based on the validation loss to avoid overfitting.

To assess the impact of each feature on the prediction outcomes, we utilized the Shapley Additive exPlanations (SHAP) method [70]. This method generates feature weights and quantifies the importance of each feature by attributing contributions to the output of the model. Based on the SHAP analysis, we identified the key features that significantly contribute to the predictive model. Using the results from the ML model, we investigated the relationship between these critical features and the target properties of ferroelectric polarizations and sliding energy barriers. Moreover, an equivariant local model was designed to accurately predict OOP by incorporating both global and local structural information derived from DFT-calculated features.

III. RESULTS

A. Geometric and electronic properties of monolayer materials

The optimized monolayer lattice constants are shown in Fig. S2(a), ranging from 2.51 to 5.41 Å. The lattice constants exhibit considerable variation among five different types. Generally, type I materials have relatively smaller lattice parameters, while type III structures have relatively larger lattice parameters. For instance, SbI₃ in type III exhibits the largest lattice parameter (5.41 Å), which is more than double that of BN (2.51 Å) in type I, with the smallest lattice parameter. In the cases where the one constituent element remains the same, the lattice constant of monolayer tends to increase with the periodic number of the other one. This trend can be attributed to the influence of atomic structure and the nature of chemical bonds on lattice parameters. The electronic structures of the monolayer materials are further calculated, including the valence-band maximum and conduction-band maximum band gap, as shown in Figs. S3 and S4. The band gaps of all monolayer materials are greater than zero, indicating their semiconductor properties.

B. OOP of homobilayer materials

Our calculations indicate that OOP occurs only in AB and BA stackings of bilayers, while AA, AA', AC, and CA stackings exhibit zero polarization. These results are consistent with previous studies showing that AB and BA stackings in 2D homobilayers have sliding ferroelectricity [25,29,35,71]. Sliding two layers of 2D materials to form either AB or BA stacking creates geometrically equivalent

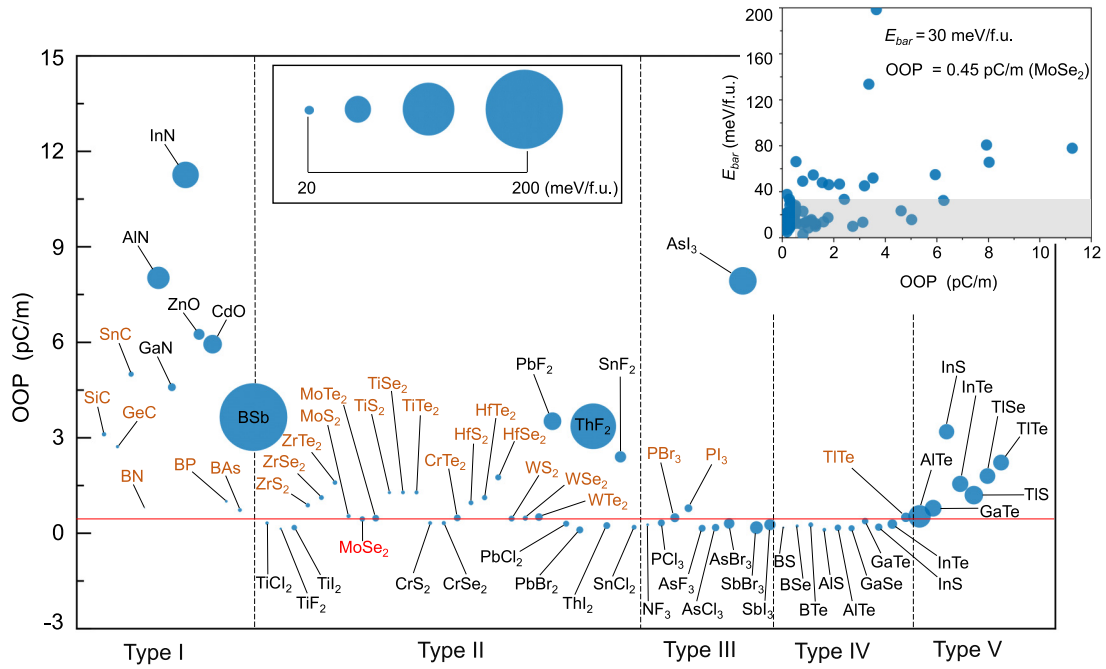


FIG. 2. The values of OOP exceeding 0.1 pC/m and corresponding sliding energy barrier of bilayer (AB/BA sliding) homobilayers, grouped into five categories. Larger spheres represent higher sliding energy barriers. The inset shows the distribution of homobilayers according to OOP and E_b . There are 25 candidates highlighted with orange (detailed in Table S1) with large OOP compared to the experimentally reported MoSe₂ (0.45 pC/m marked by a red horizontal line) and small E_b compared to the reported value of 30 meV/f.u. of yttrium-doped γ -InSe in the experiment [44].

structures [Fig. 1(c)], while with opposite polarization direction. In the rest of the paper, we thus only study AB/BA stacking for further analysis, unless otherwise specified. The lattice constants of the homobilayers with AB and BA stacking are given in Fig. S2(b), which have negligible difference. Moreover, to evaluate the stability of homobilayers, we calculate the formation energy determined by the energy difference between the homobilayers and their corresponding monolayers (Fig. S5). It is found that the calculated formation energy for all types is negative, indicating that these homobilayers are energetically favored.

Figure 2 shows the calculated OOP of identified bilayer materials (detailed in Table S1). The OOP for different types is distinct. The materials in type I exhibit the broadest distributions with variation from 0.79 to 11.30 pC/m. The large OOP are noted for some materials in type I, where InN possesses the highest value at 11.26 pC/m, followed by AlN at 8.03 pC/m, and ZnO at 6.25 pC/m, which is in good agreement with the trend reported in previous theoretical studies [25,29]. Moreover, our studies found that previously unreported CdO has a notable OOP of 5.94 pC/m. As shown in type I, most compounds composed of elements with partially filled p orbitals in the periodic table tend to exhibit relatively high OOP. This provides valuable insights for designing ferroelectric systems with large sliding ferroelectricity.

Type II has the largest number of candidates (32 over 79), including the well-established transition-metal dichalcogenides (TMDs) XY_2 ($X = \text{Mo, W}$ and $Y = \text{S, Se, Te}$) both theoretically and experimentally [17,25,34,35]. The theoretical prediction and experimental measurements of OOP for MoS₂ stand at approximately 0.97 and 0.53 pC/m,

respectively [17,25]. As shown in Fig. S1, our calculated values for MoS₂, MoSe₂, WS₂, and WSe₂ (0.45–0.54 pC/m) closely align with both the experimental values (0.51–0.53 pC/m) and the predicted values reported by Pakdel *et al.* (0.50–0.64 pC/m) using the out-of-plane polarization potential method [34,50]. Notably, other TMDs materials such as XY_2 ($X = \text{Zr, Ti, Hf}$ and $Y = \text{S, Se, Te}$) exhibit OOP values ranging from 0.88 to 1.76 pC/. In this type, the high OOP are mostly observed in fluorides, such as PbF₂, ThF₂, and SnF₂ at 3.52, 3.36, and 2.40 pC/m, respectively, yet these materials have not been experimentally reported in the literature.

Type III has a unique material, AsI₃, exhibiting a remarkable OOP of 7.93 pC/m. The OOP of AsI₃ is approximately 30% smaller than the record InN in Fig. 2. Intriguingly, it is reported that bilayer AsI₃ has shown promising performance in thermoelectric materials [59], indicating its versatility across various fields. In contrast, the rest of the materials in type III demonstrate weak OOP, all below 0.50 pC/m.

All materials in type IV exhibit small OOP, with TlTe possessing the highest value at 0.50 pC/m. Conversely, type V (the same chemical formula but with the positions of X and Y atoms exchanged from type IV) demonstrates a wide range of OOP, spanning from 0.53 to 3.91 pC/m. Besides the above important elemental factor discovered in types I, II, and III (with $Y = \text{N, F, and I}$), we find that OOP is also significantly influenced by the different configurations of identical elements in the analysis of the geometries of types IV and V. For example, in type IV, OOP for InS and InTe are recorded at 0.29 and 0.10 pC/m, respectively, while these values are enhanced to 3.19 and 1.55 pC/m with configurations in type V, respectively. This finding highlights the significant

influence of structural configurations besides the elements. Overall, these results reveal the critical role that elements and structure configurations play in determining the ferroelectric characteristics of sliding ferroelectric materials and provide insights into the design of sliding ferroelectrics and devices.

C. Sliding energy barriers for homobilayers

Besides the large out-of-plane polarization, low sliding energy barriers between AB and BA states is another important factor, essential for device applications utilizing sliding FE to achieve two states [4,35,72]. Typically, smaller energy barriers facilitate rapid polarization switching and efficient electron transfer [3,28]. In this work, we calculated the ferroelectric switching barriers from AB to BA of bilayer materials with OOP exceeding 0.1 pC/m using the CI-NEB method. Figure 2 shows calculated E_b within different types. It is found that E_b of most materials is less than 80 meV/f.u. (formula units). The experimentally reported vdW-layered yttrium-doped γ -InSe with sliding energy barrier is approximately 30 meV/f.u. [44]. Thus, we take 30 meV/f.u. as the last screening tier [Fig. 1(d)], which is potential for ferroelectric device applications. Moreover, the theoretically reported sliding energy barriers of h -BN, XY_2 ($X = \text{Mo, W}$ and $Y = \text{S, Se}$), and WTe_2 are all less than 30 meV/f.u. [34–36].

In detailed analysis in terms of types, we find that in type I, BSb has the largest barrier with 198.4 meV/f.u., potentially unsuitable for sliding FE devices. InN, AlN, ZnO, and CdO have moderate barriers of 77.9, 65.7, 32.4 and 54.9 meV/f.u., respectively. And, SiC, GeC, SnC, GaN, BN, BP, and BAs are demonstrated with low barriers of 13.4, 8.9, 15.6, and 23.3, 2.8, 8.3 and 11.7 meV/f.u., respectively. Among them, the stable sliding FE in BN has been experimentally verified [40,41]. Given the large OOP and moderate E_b under ambient conditions, there are many materials in type I with great potential for sliding FE waiting for experimental validations.

In type II, only ThF_2 has a very high energy barrier of 133.6 meV/f.u., making it unsuitable for ultrafast sliding FE applications. In contrast, PbF_2 and SnF_2 have moderate energy barriers of 52.0 and 33.2 meV/f.u., respectively. Additionally, 15 other materials exhibit OOP exceeding the experimentally reported MoSe_2 of 0.45 pC/m, with barriers below 25 meV/f.u. Our calculated largest energy barrier for TMDs of WTe_2 is approximately 22.7 meV/f.u., and it has been experimentally reported [37,38]. The other studied TMDs of XY_2 ($X = \text{Hf, Ti, Cr, Zr}$ and $Y = \text{S, Se, Te}$) show considerable potential for experimental synthesis in the field of sliding FE applications. In type III, AsI_3 shows a significant OOP with a slight high barrier of about 80.7 meV/f.u., making it worthy to try in the experiment. In spite of the low E_b , type IV materials are not suitable for ferroelectric applications due to their very small polarization. Type V materials have larger OOP but also higher barriers than type IV.

In a short summary, our comprehensive analysis offers a detailed roadmap for understanding and leveraging the sliding ferroelectric properties of various 2D materials. The identified materials, including BY ($Y = \text{N, P, As}$), XC ($X = \text{Si, Ge, Sn}$), XY_2 ($X = \text{Mo, W, Hf, Ti, Zr}$ and $Y = \text{S, Se, Te}$), CrTe_2 , PBr_3 , PI_3 , and TiTe , exhibit OOP values larger than 0.45 pC/m and energy barriers less than 30 meV/f.u., mak-

ing them favorable for sliding FE. Moreover, in addition to previously reported materials with the largest OOP more than 5 pC/m and moderate energy barriers below 80 meV/f.u., such as AlN, GaN, InN, and ZnO, we identify two materials CdO and AsI_3 which exhibit remarkable OOP values of approximately 8 pC/m, respectively. By highlighting the interplay between OOP, energy barriers, and structural configurations, the study provides valuable insights for advancing the field of sliding FE. The identified materials, with their promising OOP characteristics and suitable energy barriers, pave the way for experimental exploration and practical application in innovative ferroelectric device.

IV. DISCUSSION

A. Influencing factors on OOP

In AB/BA stacking, breaking inversion and mirror symmetries result in nonzero out-of-plane polarization, mainly driven by the distortion of atomic orbitals due to the interlayer interaction and charge transfer (CT) [25,29,31]. The interlayer coupling effect is represented by *effective* vdW radius interlayer distance ($d_{\text{vdW}}^{\text{eff}}$) (see the detailed definition of $d_{\text{vdW}}^{\text{eff}}$ in Fig. S6), the electron localization function (ELF), charge-density difference (CDD), and ion charge difference (ICD) between monolayer and corresponding bilayer. $d_{\text{vdW}}^{\text{eff}}$ corresponds to the difference between interlayer distance and the sum of the cation and anion vdW radii ($d_{\text{vdW}}^{\text{ion}}$), which can be positive or negative. Figure S6 shows the effective vdW radius representing the shortest nonbonded distance between adjacent layers, which can be used to measure the strength of interactions between layers. Generally, a larger (smaller) effective vdW radius indicates a weaker (stronger) vdW interaction.

Figure 3(a) shows the distribution of various materials on the parameter map of $d_{\text{vdW}}^{\text{eff}}$ and OOP. To some extent, the OOP tends to be higher when $d_{\text{vdW}}^{\text{eff}}$ is negative. This trend is particularly noticeable in type I. Most other types have positive $d_{\text{vdW}}^{\text{eff}}$. Interestingly, AsI_3 exhibits a high OOP but a large and positive $d_{\text{vdW}}^{\text{eff}}$ of about 2.7 Å, suggesting that its OOP is not primarily from weaker vdW interaction. Thus, we also consider other physical features, such as ELF, CDD, and ICD.

The ELF is a parameter measuring the spatial distribution of electron localization in materials, giving insight into the bonding characteristic. High ELF values (close to 1) indicate highly localized electrons, such as in covalent bonds. Intermediate ELF values (around 0.5) resemble a homogeneous electron gas. Low ELF values (close to 0) indicate low electron localization, signifying weak interactions in vdW interlayer regions. Thus, we investigate the ELF maps of AB/BA-stacked bilayer materials to explore the spatial distribution of interlayer electrons. The results are shown in Figs. S7–S11. For most materials, the results demonstrate that strong OOP aligns with higher ELF. However, types I and V include distinctive structures like BSb, AlTe, GaTe, InS, InTe, and TlSe. Despite quite noticeable ELF, these structures exhibit OOP with the highest value being only 3.65 pC/m. To quantify the interlayer ELF, we focus on the maximum interlayer ELF (ELF_{max}) located in the middle region between the lowest atoms of the upper layer and the highest atoms

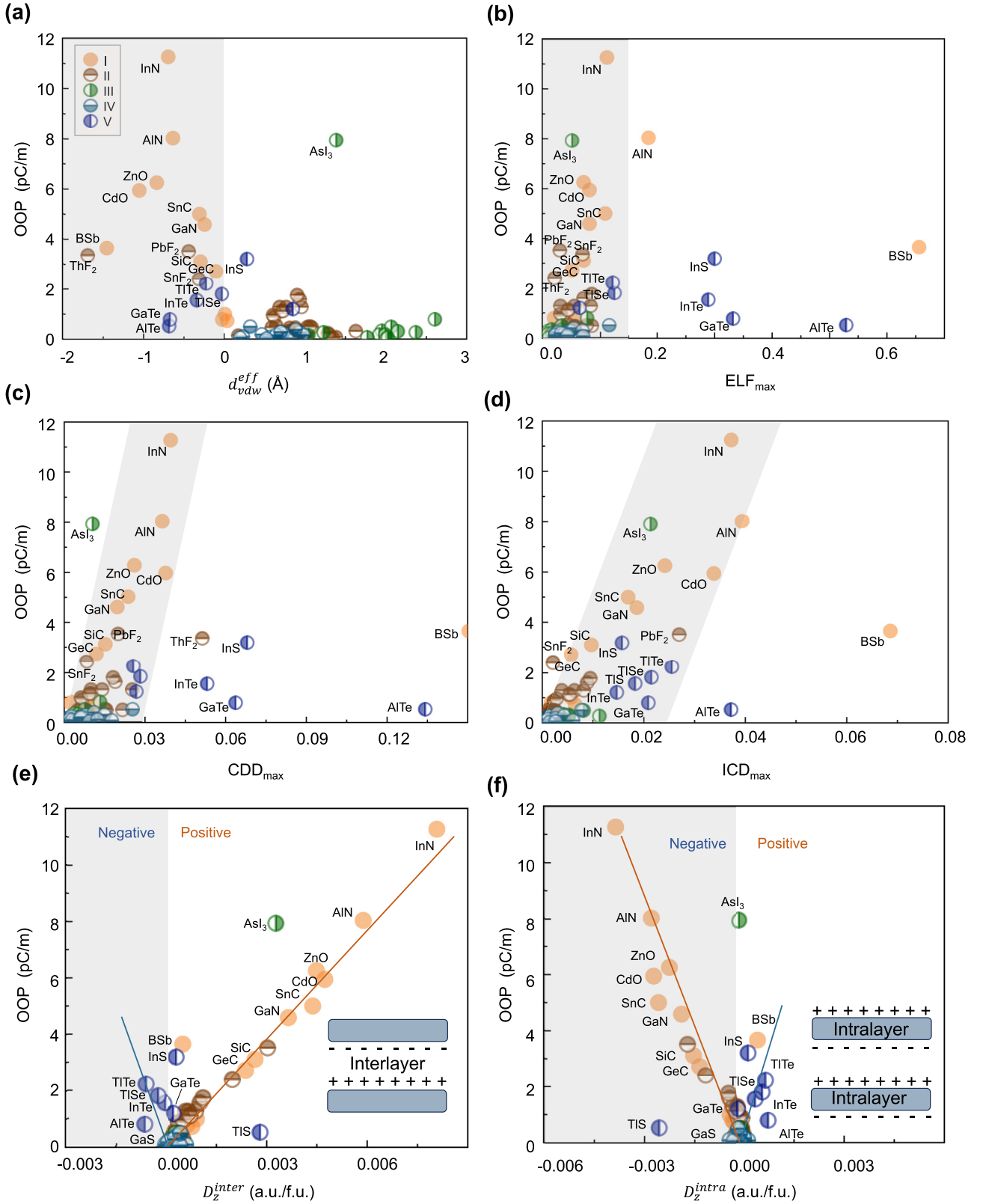


FIG. 3. (a) The OOP vs effective vdW radius interlayer distance (d_{vdw}^{eff}), (b) the interlayer maximum electron localization function (ELF_{max}), (c) the maximum average charge-density difference (CDD_{max}), and (d) the maximum absolute ion charge difference (ICD_{max}) between monolayer and corresponding bilayer. The relation between (e) interatomic dipole moment (D_z^{inter}) and (f) intra-atomic one (D_z^{intra}) dipole with OOP.

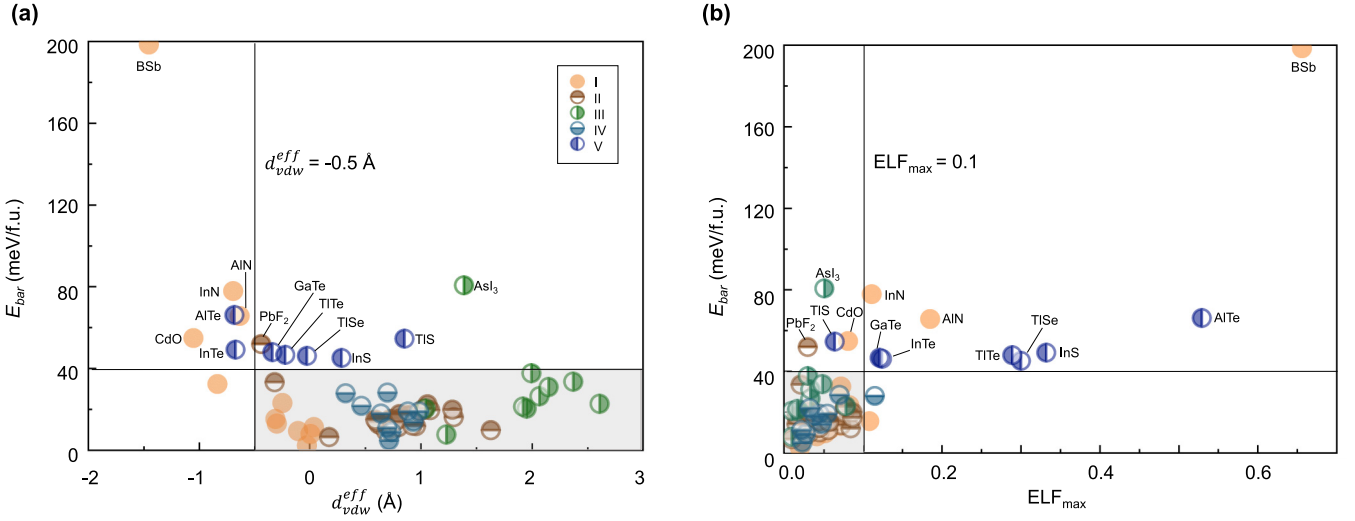


FIG. 4. The energy barrier vs (a) effective vdW radius interlayer distance ($d_{\text{vdw}}^{\text{eff}}$), and (b) the interlayer maximum electron localization function.

of the lower layer, and its correlation with OOP [Fig. 3(b)]. Most of the materials have small ELF_{max} values, less than 0.12 as shown in Fig. 3(b), indicating the weak vdW interlayer interaction. However, a few materials in types I and V (BSb, AlTe, GaTe, InS, and InTe) have ELF_{max} values exceeding 0.3. This finding indicates that ELF is an important feature to OOP but not the only one.

Figures S12–S16 show the 3D CDD maps of AB/BA-stacked bilayer materials. The results demonstrate that high OOP aligns with evident interlayer CDD for most materials. To quantify the interlayer CDD, we identified the maximum interlayer CDD (CDD_{max}) values along the z -axis average plane and correlated them with OOP, as shown in Fig. 3(c). The strength of OOP exhibits a pronounced dependence on CDD_{max} . However, noteworthy exceptions were found, with some specific systems possessing significant CDD_{max} alongside relatively low OOP, while some display substantial OOP with less evident CDD_{max} . Examples include BSb in type I, ThF₂ in type II, AsI₃ in type III, and GaTe, AlTe, InS, InTe in type V. As illustrated in Fig. 3(d), we further analyzed the relationship between OOP and the maximum ICD (ICD_{max}) between the monolayer and its corresponding bilayer. The strength of the OOP is highly dependent on ICD_{max} . Additionally, as shown in Fig. S17, our analysis reveals a consistent trend across types I–V, where anions predominantly drive CT processes in sliding ferroelectrics, except in XN ($X = \text{B, Al, Ga, In}$) and XC ($X = \text{Si, Ge, Sn}$) systems, where cations play a crucial role.

To further investigate the micromechanism underlying OOP, a decomposed scheme is proposed to isolate the interatomic dipole moment (D_z^{inter}) and intra-atomic part (D_z^{intra}) from the total polarization, as shown in Figs. 3(e) and 3(f). Remarkably, in most materials, inter- and intra-atomic components demonstrate opposite direction. However, exceptions exist for BSb in type I and InS in type V, where the inter- and intra-atomic components are aligned in the same direction. Additionally, in type V, materials such as AlTe and TlSe show a predominant intralayer component. These findings explain

why some systems, such as GaTe, InTe, and TlSe, exhibit strong ELF and CDD but relatively low overall OOP.

B. Influencing factors on sliding energy barriers

Furthermore, we investigate the relationship between energy barrier with ICD_{max} , CDD_{max} , $d_{\text{vdw}}^{\text{eff}}$, and ELF_{max} . As illustrated in Fig. S18, there is a strong correlation between the energy barrier and ICD_{max} , while the correlation with CDD_{max} is comparatively weaker. Moreover, Fig. 4(a) shows the relation between $d_{\text{vdw}}^{\text{eff}}$ and energy barrier. It is evident that when $d_{\text{vdw}}^{\text{eff}}$ is more negative, the energy barrier tends to be higher. Similarly, Fig. 4(b) shows that higher ELF_{max} values tend to higher-energy barriers. Interestingly, the clustering of data points within the shaded areas suggests that for most materials, when $d_{\text{vdw}}^{\text{eff}}$ is greater than -0.5 Å and ELF_{max} is less than 0.1, the energy barrier is below 40 meV/f.u. Recently, sliding FE in vdW-layered yttrium-doped γ -InSe has been experimentally observed with an energy barrier of approximately 30 meV/f.u. [44], localized within the clusters in Figs. 4(a) and 4(b). These findings provide valuable guidance for experimental and theoretical research, facilitating the development of materials with desired sliding ferroelectric properties.

C. Machine learning analysis

Our results indicate that OOP and the energy barrier of sliding ferroelectrics are the result of the combined effects of multiple physical quantities. Aside from the factors discussed above, the magnitude of OOP and the energy barrier should be determined by several other variables, including lattice parameters, interlayer distance, bond length, element electronegativity, vdW radius of cation and anion, and so on. For the studied stacking materials, additional effective parameters are the effective interlayer covalent bond distance ($d_{\text{int}}^{\text{eff}}$) and relative electronegativity (E_a/E_c). $d_{\text{int}}^{\text{eff}}$ is the difference between interlayer distance and bond length. E_a/E_c is defined as the electronegativity of the anion divided by that of the

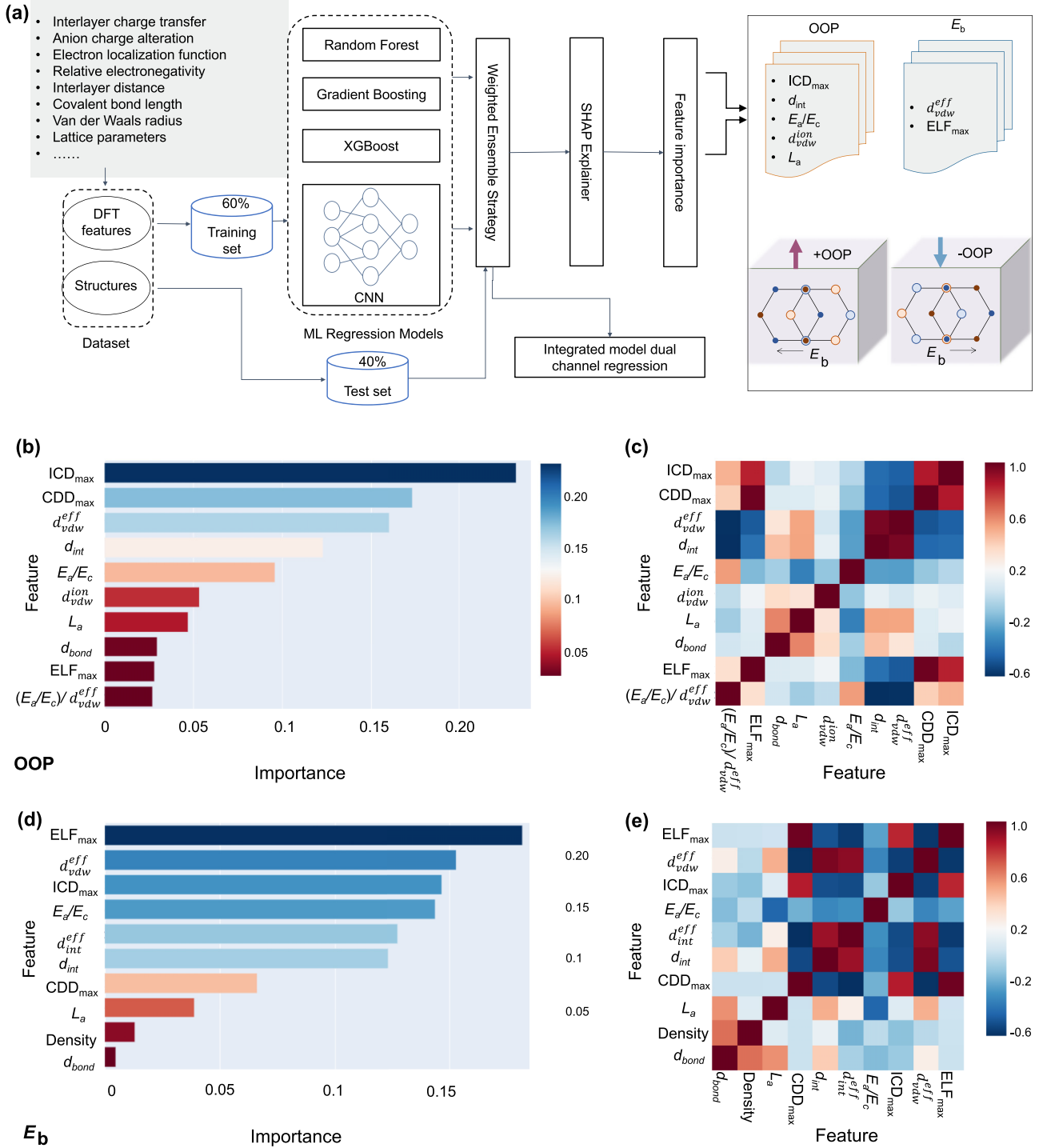


FIG. 5. (a) Overall workflow for machine learning method combined-DFT results to identify the crucial factors influencing ferroelectric polarizations and sliding energy barriers. The feature importance of (b) OOP and (d) energy barrier. The feature correlation heatmap of (c) OOP and (e) energy barrier for all the studied materials predicted by machine learning.

cation. To pinpoint the main influencers on sliding FE, we employ specific machine learning techniques to analyze the weights of various possible factors on OOP and E_b , as shown in Fig. 5(a). This allows us to establish the correlation between these factors and OOP as well as the energy barrier, providing detailed analysis of features related to the sliding ferroelectric

properties of bilayer materials. As shown in Fig. 5(b), the features are ranked by their importance in predicting OOP. This helps in understanding which features are most influential in OOP. ICD_{max} has the largest weight, followed by CDD_{max} , and then d_{vdw}^{eff} . The feature correlation heatmaps for all the studied materials are further investigated. Figure 5(c)

shows our analysis of the correlation among various features, revealing a strong positive correlation between correlation ICD_{\max} , CDD_{\max} , and ELF_{\max} , as well as between $d_{\text{vdW}}^{\text{eff}}$ and d_{int} , and an evident negative correlation between ICD_{\max} (CDD_{\max} , ELF_{\max}) and $d_{\text{vdW}}^{\text{eff}}$ (d_{int}). Based on the above critical feature analysis, we selected the main factors to establish a general relationship among them, as given in Fig. S19. After linear fitting, the R -squared value for this relationship is approximately 0.87. OOP is positively proportional to ICD_{\max} and the relative electronegativity difference between the cation and anion. Conversely, it is inversely proportional to the ratio of the interlayer distance to the sum of the vdW radii of the cation and anion, as well as to the unit-cell area. Moreover, the key influencing factors for energy barrier are also identified by ML techniques. As depicted in Fig. 5(d), the ELF_{\max} has the largest weight for energy barrier, followed by $d_{\text{vdW}}^{\text{eff}}$ and then ICD_{\max} . Given the strong correlation between ELF_{\max} and ICD_{\max} , as shown in Fig. 5(e), our ML results have a good agreement with that of our DFT, that the key influencing factors for energy barrier are mainly $d_{\text{vdW}}^{\text{eff}}$ and ELF_{\max} .

As discussed above, the out-of-plane polarization is influenced by multiple factors, including charge transfer, interlayer distance, element electronegativity, van der Waals radii, unit-cell area, etc. This complexity indicates the need for a more nuanced approach to capture the local interfacial physics. To address this, we designed an equivariant local model to accurately predict OOP by incorporating both global and local structural information derived from DFT-calculated features. Our approach involves encoding DFT-computed features and structural descriptors into two distinct embedding spaces, representing global and local information separately. These embeddings are processed through a series of three equivariant modules, each designed to preserve physical symmetries by maintaining invariance under rotations and translations, as shown in Fig. 6(a). This ensures that the fundamental physical properties of the system are respected. Following the equivariant modules, the output is passed through an Adaptive Local Environment module, which is specifically designed to capture key interface characteristics of the heterostructure. Finally, a decoder network refines and processes the features to generate the predicted OOP values. This architecture leverages the strengths of equivariant learning to maintain physical invariances while adapting to the complex local environments at heterostructure interfaces. To expand the dataset, we selected stable AB/BA-stacked honeycomb bilayer structures from the Computational Bilayer Database (BIDB) [50] and calculated the OOP using the Berry-phase method. The predicted OOP values from our machine learning model, alongside the calculated values, are presented in Fig. 6(b). The predicted mean absolute error is 0.11 pC/m, demonstrating the model's reliability in predicting OOP. By addressing the unique challenges of sliding ferroelectric materials, this model provides more accurate and detailed predictions of their behavior.

V. CONCLUSIONS

Through high-throughput DFT calculations, we identified 25 bilayer honeycomb homobilayers of sliding ferroelectrics that have large out-of-plane polarization and low sliding en-

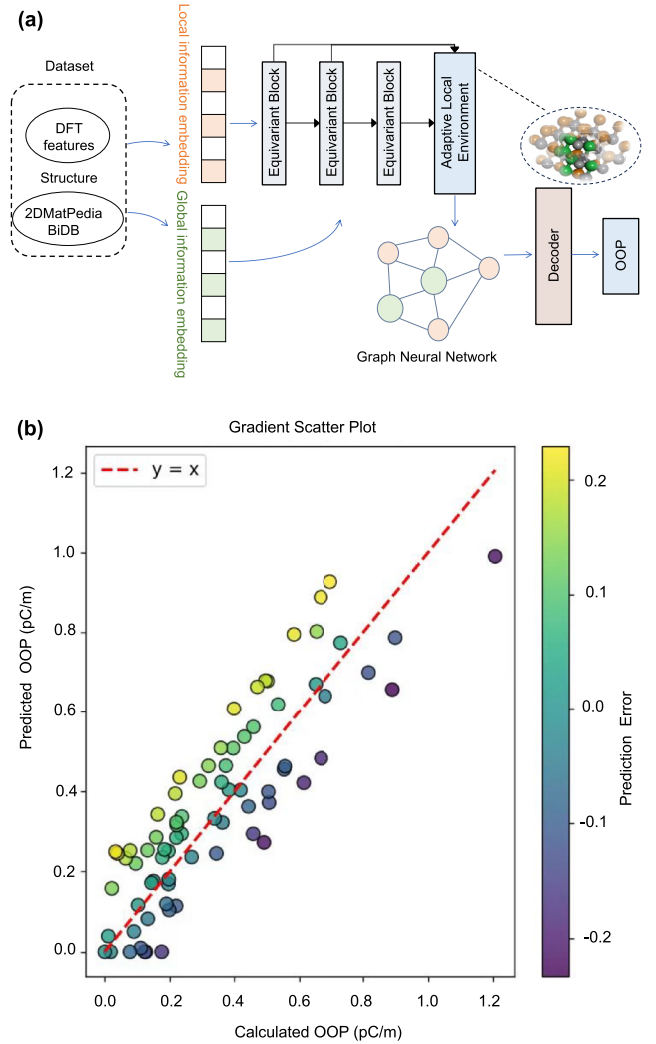


FIG. 6. (a) Overall workflow for machine learning regression method with equivariant local model. (b) The relationship between the calculated OOP and the predicted OOP values based on the Computational Bilayer Database (BIDB).

ergy barriers. These high-performance sliding ferroelectrics include previously reported materials, such as AlN, GaN, InN, ZnO, h -BN, and MoS₂, as well as two identified materials, CdO and AsI₃, with remarkable OOP. A comprehensive big-data driven physical analysis reveals that OOP is strongly correlated with five key factors: effective vdW radius, relative electronegativity, interlayer distance, charge transfer, and unit-cell area. Moreover, the effective vdW radius is also a critical factor in determining the sliding energy barrier, together with the maximum interlayer electron localization function. Finally, we performed machine learning techniques to weight these physical features and predict sliding ferroelectric properties. Our findings provide deeper insights into the underlying mechanisms and offer valuable theoretical guidance for the rational design of high-performance sliding ferroelectrics and related experimental devices.

ACKNOWLEDGMENTS

L.S. acknowledges the financial support from Singapore MOE Tier 1 (Grant No. A-8001194-00-00) and Singapore MOE Tier 2 (Grant No. A-8001872-00-00); X.S.W. and L.S. acknowledge the financial support from Singapore MOE Tier 1 (Grant No. 23-0450-A0001); and J.Y. acknowledges the

National Natural Science Foundation of China (Grant No. 12404286).

DATA AVAILABILITY

The data supporting this study's findings are available within the article.

- [1] J. S. Meena, S. M. Sze, U. Chand, and T.-Y. Tseng, Overview of emerging nonvolatile memory technologies, *Nanoscale Res. Lett.* **9**, 526 (2014).
- [2] Y. Chen, B. Zhang, G. Liu, X. Zhuang, and E.-T. Kang, Graphene and its derivatives: Switching ON and OFF, *Chem. Soc. Rev.* **41**, 4688 (2012).
- [3] M. Wu and J. Li, Sliding ferroelectricity in 2D van der Waals materials: Related physics and future opportunities, *Proc. Natl. Acad. Sci. USA* **118**, e2115703118 (2021).
- [4] C. Fox, Y. Mao, X. Zhang, Y. Wang, and J. Xiao, Stacking order engineering of two-dimensional materials and device applications, *Chem. Rev.* **124**, 1862 (2023).
- [5] S. Li, F. Wang, Y. Wang, J. Yang, X. Wang, X. Zhan, J. He, and Z. Wang, Van der Waals ferroelectrics: Theories, materials, and device applications, *Adv. Mater.* **36**, 2301472 (2024).
- [6] W. Sun, W. Wang, R. Hu, C. Yang, S. Huang, X. Li, and Z. Cheng, Ultra-high-density ferroelectric array formed by sliding ferroelectric moiré superlattices, *Nano Lett.* **23**, 11280 (2023).
- [7] N. Sai, A. M. Kolpak, and A. M. Rappe, Ferroelectricity in ultrathin perovskite films, *Phys. Rev. B* **72**, 020101(R) (2005).
- [8] J. Junquera and P. Ghosez, Critical thickness for ferroelectricity in perovskite ultrathin films, *Nature (London)* **422**, 506 (2003).
- [9] K. J. Choi, M. Biegalski, Y. L. Li, A. Sharan, J. Schubert, R. Uecker, P. Reiche, Y. B. Chen, X. Q. Pan, V. Gopalan *et al.*, Enhancement of ferroelectricity in strained BaTiO₃ thin films, *Science* **306**, 1005 (2004).
- [10] J. F. Scott, Applications of modern ferroelectrics, *Science* **315**, 954 (2007).
- [11] S. Bertolazzi, P. Bondavalli, S. Roche, T. San, S. Y. Choi, L. Colombo, F. Bonaccorso, and P. Samorì, Nonvolatile memories based on graphene and related 2D materials, *Adv. Mater.* **31**, 1806663 (2019).
- [12] J. Wu, H. Y. Chen, N. Yang, J. Cao, X. Yan, F. Liu, Q. Sun, X. Ling, J. Guo, and H. Wang, High tunneling electroresistance in a ferroelectric van der Waals heterojunction via giant barrier height modulation, *Nat. Electron.* **3**, 466 (2020).
- [13] C. Wang, L. You, D. Cobden, and J. Wang, Towards two-dimensional van der Waals ferroelectrics, *Nat. Mater.* **22**, 542 (2023).
- [14] L. Ju, Z. Shi, N. Nair, Y. Lv, C. Jin, J. Velasco Jr, C. Ojeda-Aristizabal, H. A. Bechtel, M. C. Martin, A. Zettl *et al.*, Topological valley transport at bilayer graphene domain walls, *Nature (London)* **520**, 650 (2015).
- [15] R. Ramesh and N. A. Spaldin, Multiferroics: Progress and prospects in thin films, *Nat. Mater.* **6**, 21 (2007).
- [16] R. C. Xiao, Y. Gao, H. Jiang, W. Gan, C. Zhang, and H. Li, Non-synchronous bulk photovoltaic effect in two-dimensional interlayer-sliding ferroelectrics, *npj Comput. Mater.* **8**, 138 (2022).
- [17] S. Deb, W. Cao, N. Raab, K. Watanabe, T. Taniguchi, M. Goldstein, L. Kronik, M. Urbakh, O. Hod, and M. Ben Shalom, Cumulative polarization in conductive interfacial ferroelectrics, *Nature (London)* **612**, 465 (2022).
- [18] P. Ghosez and K. M. Rabe, Microscopic model of ferroelectricity in stress-free PbTiO₃ ultrathin films, *Appl. Phys. Lett.* **76**, 2767 (2000).
- [19] K. F. Mak, C. Lee, J. Hone, J. Shan, and T. F. Heinz, Atomically thin MoS₂: A new direct-gap semiconductor, *Phys. Rev. Lett.* **105**, 136805 (2010).
- [20] K. S. Novoselov, D. Jiang, F. Schedin, T. J. Booth, V. V. Khotkevich, S. V. Morozov, and A. K. Geim, Two-dimensional atomic crystals, *Proc. Natl. Acad. Sci. USA* **102**, 10451 (2005).
- [21] A. Belianinov, Q. He, A. Dziazgys, P. Maksymovych, E. Eliseev, A. Borisevich, A. Morozovska, J. Banys, Y. Vysokhanskii, and S. V. Kalinin, CuInP₂S₆ room temperature layered ferroelectric, *Nano Lett.* **15**, 3808 (2015).
- [22] Y. Zhou, D. Wu, Y. Zhu, Y. Cho, Q. He, X. Yang, K. Herrera, Z. Chu, Y. Han, M. C. Downer *et al.*, Out-of-plane piezoelectricity and ferroelectricity in layered α -In₂Se₃ nanoflakes, *Nano Lett.* **17**, 5508 (2017).
- [23] S. Yuan, X. Luo, H. L. Chan, C. Xiao, Y. Dai, M. Xie, and J. Hao, Room-temperature ferroelectricity in MoTe₂ down to the atomic monolayer limit, *Nat. Commun.* **10**, 1775 (2019).
- [24] M. Kruse, U. Petralanda, M. N. Gjerding, K. W. Jacobsen, K. S. Thygesen, and T. Olsen, Two-dimensional ferroelectrics from high-throughput computational screening, *npj Comput. Mater.* **9**, 45 (2023).
- [25] L. Li and M. Wu, Binary compound bilayer and multilayer with vertical polarizations: Two-dimensional ferroelectrics, multiferroics, and nanogenerators, *ACS Nano* **11**, 6382 (2017).
- [26] S. Assavachin and F. E. Osterloh, Ferroelectric polarization in BaTiO₃ nanocrystals controls photoelectrochemical water oxidation and photocatalytic hydrogen evolution, *J. Am. Chem. Soc.* **145**, 18825 (2023).
- [27] Y. Li, Y. Jin, X. Lu, J. C. Yang, Y. H. Chu, F. Huang, J. Zhu, and S. W. Cheong, Rewritable ferroelectric vortex pairs in BiFeO₃, *npj Comput. Mater.* **2**, 43 (2017).
- [28] M. Wu, Two-dimensional van der Waals ferroelectrics: Scientific and technological opportunities, *ACS Nano* **15**, 9229 (2021).
- [29] Z. Wang, Z. Gui, and L. Huang, Sliding ferroelectricity in bilayer honeycomb structures: A first-principles study, *Phys. Rev. B* **107**, 035426 (2023).
- [30] Z. Lin, C. Si, S. Duan, C. Wang, and W. Duan, Rashba splitting in bilayer transition metal dichalcogenides controlled by electronic ferroelectricity, *Phys. Rev. B* **100**, 155408 (2019).
- [31] Q. Yang, M. Wu, and J. Li, Origin of two-dimensional vertical ferroelectricity in WTe₂ bilayer and multilayer, *J. Phys. Chem. Lett.* **9**, 7160 (2018).

- [32] X. Liu, A. P. Pyatakov, and W. Ren, Magnetoelectric coupling in multiferroic bilayer VS_2 , *Phys. Rev. Lett.* **125**, 247601 (2020).
- [33] N. Ding, J. Chen, C. Gui, H. You, X. Yao, and S. Dong, Phase competition and negative piezoelectricity in interlayer-sliding ferroelectric ZrI_2 , *Phys. Rev. Mater.* **5**, 084405 (2021).
- [34] X. Wang, K. Yasuda, Y. Zhang, S. Liu, K. Watanabe, T. Taniguchi, J. Hone, L. Fu, and P. Jarillo-Herrero, Interfacial ferroelectricity in rhombohedral-stacked bilayer transition metal dichalcogenides, *Nat. Nanotechnol.* **17**, 367 (2022).
- [35] P. Meng, Y. Wu, R. Bian, E. Pan, B. Dong, X. Zhao, J. Chen, L. Wu, Y. Sun, Q. Fu *et al.*, Sliding induced multiple polarization states in two-dimensional ferroelectrics, *Nat. Commun.* **13**, 7696 (2022).
- [36] H. Jiang, L. Li, Y. Wu, R. Duan, K. Yi, L. Wu, C. Zhu, L. Luo, M. Xu, L. Zheng *et al.*, Vapor deposition of bilayer 3R MoS_2 with room-temperature ferroelectricity, *Adv. Mater.* **36**, 2400670 (2024).
- [37] Z. Fei, W. Zhao, T. A. Palomaki, B. Sun, M. K. Miller, Z. Zhao, J. Yan, X. Xu, and D. H. Cobden, Ferroelectric switching of a two-dimensional metal, *Nature (London)* **560**, 336 (2018).
- [38] J. Xiao, Y. Wang, H. Wang, C. D. Pemmaraju, S. Wang, P. Muscher, E. J. Sie, C. M. Nyby, T. P. Devereaux, X. Qian *et al.*, Berry curvature memory through electrically driven stacking transitions, *Nat. Phys.* **16**, 1028 (2020).
- [39] W. Hou, A. Azizimanesh, A. Sewaket, T. Peña, C. Watson, M. Liu, H. Askari, and S. M. Wu, Strain-based room-temperature non-volatile MoTe_2 ferroelectric phase change transistor, *Nat. Nanotechnol.* **14**, 668 (2019).
- [40] K. Yasuda, X. Wang, K. Watanabe, T. Taniguchi, and P. Jarillo-Herrero, Stacking-engineered ferroelectricity in bilayer boron nitride, *Science* **372**, 1458 (2021).
- [41] M. Vizner Stern, Y. Waschitz, W. Cao, I. Nevo, K. Watanabe, T. Taniguchi, E. Sela, M. Urbakh, O. Hod, and M. Ben Shalom, Interfacial ferroelectricity by van der Waals sliding, *Science* **372**, 1462 (2021).
- [42] Y. Wan, T. Hu, X. Mao, J. Fu, K. Yuan, Y. Song, X. Gan, X. Xu, M. Xue, X. Cheng *et al.*, Room-temperature ferroelectricity in $1\text{T}'\text{-ReS}_2$ multilayers, *Phys. Rev. Lett.* **128**, 067601 (2022).
- [43] F. Sui, M. Jin, Y. Zhang, R. Qi, Y. N. Wu, R. Huang, F. Yue, and J. Chu, Sliding ferroelectricity in van der Waals layered $\gamma\text{-InSe}$ semiconductor, *Nat. Commun.* **14**, 36 (2023).
- [44] F. Sui, H. Li, R. Qi, M. Jin, Z. Lv, M. Wu, X. Liu, Y. Zheng, B. Liu, R. Ge *et al.*, Atomic-level polarization reversal in sliding ferroelectric semiconductors, *Nat. Commun.* **15**, 3799 (2024).
- [45] H. Hu, Y. Sun, M. Chai, D. Xie, J. Ma, and H. Zhu, Room-temperature out-of-plane and in-plane ferroelectricity of two-dimensional $\beta\text{-InSe}$ nanoflakes, *Appl. Phys. Lett.* **114**, 252903 (2019).
- [46] R. Bian, G. Cao, E. Pan, Q. Liu, Z. Li, L. Liang, Q. Wu, L. K. Ang, W. Li, X. Zhao *et al.*, High-performance sliding ferroelectric transistor based on Schottky barrier tuning, *Nano Lett.* **23**, 4595 (2023).
- [47] W. Li, X. Zhang, J. Yang, S. Zhou, C. Song, P. Cheng, Y.-Q. Zhang, B. Feng, Z. Wang, Y. Lu, K. Wu *et al.*, Emergence of ferroelectricity in a nonferroelectric monolayer, *Nat. Commun.* **14**, 2757 (2023).
- [48] M. Liu, J. Gou, Z. Liu, Z. Chen, Y. Ye, J. Xu, X. Xu, D. Zhong, G. Eda, and A. T. S. Wee, Phase-selective in-plane heteroepitaxial growth of H-phase CrSe_2 , *Nat. Commun.* **15**, 1765 (2024).
- [49] A. Zavabeti, A. Jannat, L. Zhong, A. A. Haidry, Z. Yao, and J. Z. Ou, Two-dimensional materials in large areas: Synthesis, properties, and applications, *Nat. Commun.* **12**, 66 (2020).
- [50] S. Pakdel, A. Rasmussen, A. Taghizadeh, M. Kruse, T. Olsen, and K. S. Thygesen, High-throughput computational stacking reveals emergent properties in natural van der Waals bilayers, *Nat. Commun.* **15**, 932 (2024).
- [51] J. Zhou, L. Shen, M. D. Costa, K. A. Persson, S. P. Ong, Y. Lu, X. Ma, Y. Chen, H. Tang, and Y. P. Feng, 2D MatPedia, an open computational database of two-dimensional materials from top-down and bottom-up approaches, *Sci. Data* **6**, 86 (2019).
- [52] J. Zhou, J. Lin, X. Huang, Y. Zhou, Y. Chen, J. Xia, H. Wang, Y. Xie, H. Yu, J. Lei *et al.*, A library of atomically thin metal chalcogenides, *Nature (London)* **556**, 355 (2018).
- [53] D. Pacile, J. Meyer, Ç. Girit, and A. Zettl, The two-dimensional phase of boron nitride: Few-atomic-layer sheets and suspended membranes, *Appl. Phys. Lett.* **92**, 133107 (2008).
- [54] J. Jiang, L. Xu, C. Qiu, and L.-M. Peng, Ballistic two-dimensional InSe transistors, *Nature (London)* **616**, 470 (2023).
- [55] T.-R. Wei, M. Jin, Y. Wang, H. Chen, Z. Gao, K. Zhao, P. Qiu, Z. Shan, J. Jiang *et al.*, Exceptional plasticity in the bulk single-crystalline van der Waals semiconductor InSe , *Science* **369**, 542 (2020).
- [56] M. Yu, S. A. Iddawela, J. Wang, M. Hilse, J. L. Thompson, D. R. Hickey, S. B. Sinnott, and S. Law, Quasi-van der Waals epitaxial growth of $\gamma'\text{-GaSe}$ nanometer-thick films on GaAs (111) B substrates, *ACS Nano* **18**, 17185 (2024).
- [57] L. C. Muhimmah and C.-H. Ho, Dual phase two-color emission observed in van der Waals GaTe planes, *Appl. Surf. Sci.* **542**, 148593 (2021).
- [58] J. Fu, M. Kuisma, A. H. Larsen, K. Shinohara, A. Togo, and K. S. Thygesen, Symmetry classification of 2D materials: Layer groups versus space groups, *2D Mater.* **11**, 035009 (2024).
- [59] Q. Tang, S. Han, M. Yao, D. J. Singh, J. Xi, H. Liu, and J. Yang, Enhancing the electrical transport properties of two-dimensional semiconductors through interlayer interactions, *Energy Environ. Sci.* **17**, 611 (2024).
- [60] G. Kresse and J. Furthmüller, Efficient iterative schemes for *ab initio* total-energy calculations using a plane-wave basis set, *Phys. Rev. B* **54**, 11169 (1996).
- [61] G. Kresse and J. Furthmüller, Efficiency of *ab initio* total energy calculations for metals and semiconductors using a plane-wave basis set, *Comput. Mater. Sci.* **6**, 15 (1996).
- [62] P. E. Blöchl, Projector augmented-wave method, *Phys. Rev. B* **50**, 17953 (1994).
- [63] J. P. Perdew, K. Burke, and M. Ernzerhof, Generalized gradient approximation made simple, *Phys. Rev. Lett.* **77**, 3865 (1996).
- [64] H. J. Monkhorst and J. D. Pack, Special points for Brillouin-zone integrations, *Phys. Rev. B* **13**, 5188 (1976).
- [65] D. Sheppard, P. Xiao, W. Chemelewski, D. D. Johnson, and G. Henkelman, A generalized solid-state nudged elastic band method, *J. Chem. Phys.* **136**, 074103 (2012).
- [66] S. Grimme, S. Ehrlich, and L. Goerigk, Effect of the damping function in dispersion corrected density functional theory, *J. Comput. Chem.* **32**, 1456 (2011).
- [67] R. D. King-Smith and D. Vanderbilt, Theory of polarization of crystalline solids, *Phys. Rev. B* **47**, 1651 (1993).

- [68] See Supplemental Material at <http://link.aps.org/supplemental/10.1103/PhysRevB.111.094106> for the OOP polarization and sliding energy barriers of bilayer homo-structures, covering structural parameters, electronic properties, binding energy, ELF, CDD, ICD, their correlation with key factors, and which includes Refs. [25,29,34,40,50,73,74].
- [69] I. O. Tolstikhin, N. Houlsby, A. Kolesnikov, L. Beyer, X. Zhai, T. Unterthiner, J. Yung, A. Steiner, D. Keysers, J. Uszkoreit, M. Lucic, and A. Dosovitski, MLP-mixer: An all-MLP architecture for vision, [arXiv:2105.01601](https://arxiv.org/abs/2105.01601).
- [70] S.M. Lundberg and S.-I. Lee, A unified approach to interpreting model predictions, [arXiv:1705.07874](https://arxiv.org/abs/1705.07874).
- [71] K. Liu, X. Ma, S. Xu, and M. Zhao, Tunable sliding ferroelectricity and magnetoelectric coupling in two-dimensional multiferroic MnSe material, *npj Comput. Mater.* **9**, 16 (2023).
- [72] Z. Zheng, Q. Ma, Z. Bi, S. de la Barrera, M.-H. Liu, N. Mao, Y. Zhang, N. Kiper, K. Watanabe, T. Taniguchi, J. Kong, W. A. Tisdale, R. Ashoori, N. Gedik, L. Fu, S.-Y. Xu, and P. Jarillo-Herrero, Unconventional ferroelectricity in moiré heterostructures, *Nature (London)* **588**, 71 (2020).
- [73] F. L. Hirshfeld, Bonded-atom fragments for describing molecular charge densities, *Theor. Chim. Acta* **44**, 129 (1977).
- [74] C. C. J. Roothaan, New developments in molecular orbital theory, *Rev. Mod. Phys.* **23**, 69 (1951).